

# An Eulerian Quantum Neural Network for Image Classification

Soumyadip Sahoo

*dept. name of organization (of Aff.)*

*name of organization (of Aff.)*

City, Country

email address or ORCID

Diptarka Mandal

*dept. name of organization (of Aff.)*

*name of organization (of Aff.)*

City, Country

email address or ORCID

Asfak Ali

*dept. name of organization (of Aff.)*

*name of organization (of Aff.)*

City, Country

email address or ORCID

Dmitrii Kaplun

*dept. name of organization (of Aff.)*

*name of organization (of Aff.)*

City, Country

email address or ORCID

Given Name Surname

*dept. name of organization (of Aff.)*

*name of organization (of Aff.)*

City, Country

email address or ORCID

Ram Sarkar

*dept. name of organization (of Aff.)*

*name of organization (of Aff.)*

City, Country

email address or ORCID

**Abstract**—Recent advancements in deep learning (DL) have significantly improved image classification techniques across various domains such as healthcare, security, and autonomous systems. However, the computational complexity of classical DL models poses substantial challenges, requiring extensive resources like - large dataset\*, computational time\* for training and inference, which limits their applicability in resource-constrained environments. Quantum Machine Learning (QML) has emerged as a promising alternative by leveraging the principles of quantum mechanics—such as superposition and entanglement—to facilitate efficient data processing within the Hilbert space. In this work, we propose the Eulerian Quantum Neural Network (EQNN), a quantum-based deep learning model that employs Eulerian rotational unitary matrices to achieve robust quantum feature representation using quantum gates, ensuring improved data fidelity. The proposed framework incorporates unitary operations and controlled Pauli-Z gates to extract classical insights from quantum data, enabling seamless integration with existing classical systems. Besides computationally efficient solution for image classification, the EQNN’s performance evaluation on the MNIST, F-MNIST, and P-MNIST datasets demonstrates the model’s effectiveness in both binary and multi-class classification tasks, achieving promising results even with a limited number of trainable parameters. These findings highlight the potential of EQNN as a resource-efficient and scalable approach for next-generation image classification systems.

**Index Terms**—Quantum Machine Learning, Quantum Computing, Hilbert space, Deep Learning, Image Classification, Euler Angle

## I. INTRODUCTION

Recent progress in machine learning\* (ML) and deep learning\* (DL) has created numerous opportunities for tackling previously unresolved challenges. From low-dimensional tabular data to high-dimensional image and video data, DL enables effective analysis and decision-making. In many tasks, DL models have surpassed human-level performance. One of them is image classification, which has become a pivotal component of modern computer vision, enabling the automatic categorization of visual data across diverse applications. The advent

of DL, particularly convolutional neural networks (CNNs), has significantly enhanced the accuracy and scalability of image classification systems by enabling models to extract and learn complex hierarchical features directly from data. These advancements have facilitated transformative applications, including disease diagnosis in medical imaging\*, real-time object recognition in autonomous vehicles\*, and remote sensing\* for environmental monitoring. The adaptability and precision of DL-based image classification have made it a cornerstone technology in industries such as healthcare, security, e-commerce and many more.

Classical models demand significant computational resources and time for both training and inference. For instance, one of the latest visual transformer [4] architectures trained on the ImageNet dataset contains over 2 billion\* parameters and required more than 10,000 TPU core-days for training. Classical ML models focus on minimizing empirical risk and sample complexity; however, they often struggle with generalization, especially when trained on limited data. A well-balanced model must optimize empirical risk, increase generalization ability, and reduce sample complexity to ensure reliable performance on unseen data [9].

In current years, Quantum Machine Learning (QML)\* with its ability to utilize the principles of quantum mechanics [6] like superposition and entanglement offers new possibilities for overcoming these barriers [11]. ML models are traditionally trained in Euclidean space, latent space, and manifold space, whereas quantum computing operates in the Hilbert space, enabling accurate classifications with fewer training samples. Recent advancements in Noisy Intermediate-Scale Quantum (NISQ)\* devices have made it feasible to explore hybrid quantum-classical models that can leverage the strengths of both paradigms [13]. Quantum algorithms, such as quantum support vector machines and variational quantum circuits, promise to improve the optimization processes underlying model training. While still in its early development, QML

has demonstrated the potential to overcome the bottlenecks associated with classical approaches, including interpretability challenges, time complexity and computational inefficiencies, making it a compelling avenue for next-generation image classification systems [10].

**Motivation and Contributions:** Euler angles play a fundamental role in both classical and quantum mechanics, offering a robust framework for describing rotations in multidimensional spaces. In quantum computing\*, they are particularly valuable for representing unitary operations on qubits, facilitating efficient manipulation of quantum states within the Bloch sphere\*. Unlike simpler rotational models, Euler angles provide a comprehensive means of encoding rotational symmetries and transformations, making them essential for tasks involving angular momentum and state evolution in quantum systems. Furthermore, the non-commutative nature of 3D rotations necessitates the use of three independent angles to fully capture the orientation of a system without ambiguities or singularities. Motivated by these facts, our proposed **Eulerian Quantum Neural Network (EQNN)** model integrates Euler angle rotations using a minimal qubit requirement to achieve efficient and accurate classification of image data. By leveraging unitary matrices and controlled Pauli-Z gates, the model ensures high-fidelity quantum data representation while maintaining computational efficiency. The **highlighting** points of this work are as follows:

- **Efficient Quantum Representation:** The proposed QENN model employs Euler angles for precise quantum state transformations, ensuring comprehensive representation of image data with only 16 qubits.
- **Lightweight Design:** Our approach offers competitive performance in both binary and multi-class classification tasks while requiring minimal training data and computational resources in comparison with traditional deep learning techniques\*.
- **Enhanced Measurement Strategy:** By utilizing the Pauli-Z gate for measurement, the model effectively bridges the gap between quantum and classical data representations, facilitating accurate extraction of useful features.
- **Robust Model:** We have evaluated our proposed EQNN on three benchmark datasets (MNIST, F-MNIST, and P-MNIST) for both binary and multiclass classification tasks, achieving promising accuracy.

## II. LITERATURE SURVEY

The advent of QML has introduced novel paradigms for solving computationally intensive problems, particularly in the domain of image classification. By harnessing the principles of quantum mechanics, QML models aim to overcome the limitations of classical machine learning approaches in terms of computational scalability and efficiency. Recent advancements in hybrid quantum-classical architectures and fully quantum models have demonstrated significant potential for applications in image classification, leveraging the unique properties of quantum systems such as superposition, entanglement, and

quantum interference. In the following, we review some of the key contributions in this rapidly evolving field.

Cong et al. (2019) [3] introduced Quantum Convolutional Neural Networks (QCNNs), inspired by classical CNNs, to efficiently process quantum data. QCNNs utilize  $O(\log(N))$  variational parameters for  $N$  qubits, enabling scalable training on near-term quantum devices. This model integrates the multi-scale entanglement renormalization ansatz and quantum error correction, demonstrating its utility in recognizing quantum states in 1D symmetry-protected topological phases and optimizing error correction schemes. The work highlighted the potential of QCNNs in advancing quantum state analysis and scalable machine learning frameworks.

Henderson et al. (2019) [7] extended the application of quantum neural networks by proposing Quconvolutional Neural Networks (QNNs), which embed quantum convolutional layers within classical CNNs. These quconvolutional layers apply random quantum circuits to locally transform input data, analogous to the operations in classical convolutional layers. Experiments on the MNIST dataset revealed that QNNs achieve higher test accuracy and faster training compared to classical CNNs, with minimal quantum circuit requirements and no reliance on quantum error correction.

LaRose and Coyle (2019) [8] explored robust data encodings for binary quantum classification, emphasizing their importance in noise-resilient quantum machine learning. The study demonstrated how data encodings influence learnable decision boundaries and affect classification stability under noise. By introducing robust encodings and providing theoretical guarantees, the authors illustrated the impact of encoding strategies on improving quantum classifier performance, particularly in noisy environments.

Chalumuri et al. (2021) [2] proposed a hybrid quantum-classical architecture for image scene classification, where quantum computation was employed for feature extraction and classical computation for classification. This architecture, tested on the IBM\_santiago quantum computer, reduced the number of trainable parameters by approximately 27–30% compared to classical state-of-the-art models. Achieving classification accuracies of 95.89%, 86.13%, and 79.32% on the UC Merced Land-Use, AID, and NWPU-RESISC45 datasets, respectively, this work showcased the efficiency of hybrid quantum models in maintaining high performance while reducing training complexity.

Saxena and Nigam (2021) [12] investigated the performance of Variational Quantum Classifiers (VQCs), a hybrid quantum-classical model for binary classification tasks. Utilizing quantum properties such as entanglement and superposition, the VQC achieved classification accuracies comparable to classical models on the Iris dataset using only four qubits. This study highlighted the potential of VQCs in addressing classification problems with computational efficiency, especially in the NISQ era.

Philip et al. (2022) [5] introduced a novel single-qubit-based deep quantum neural network for image classification. By mimicking classical CNN techniques, this model significantly

reduced the number of trainable parameters while maintaining high performance. Tested on datasets such as MNIST, Fashion-MNIST, and ORL face datasets, the proposed architecture achieved promising accuracies of 94.6%, 89.5%, and 82.5%, respectively. The study demonstrated the potential of deep QNNs in scalable QML applications, especially under noisy simulation environments.

Collectively, the above study highlights the transformative potential of QML models in image classification. By leveraging quantum computational advantages, these approaches not only address scalability and efficiency challenges but also pave the way for further advancements in quantum-enhanced data analysis and decision-making systems.

### III. METHODS AND MATERIALS

In quantum mechanics, rotations in 3D space are described using the rotation operators that act on quantum states, particularly those associated with angular momentum. Rotational angles  $(\phi, \theta, \psi)$  are used to parametrize these rotations. Rotation operators are given by:

$$R_x(\phi) = e^{-i\phi\hat{J}_x}; \quad R_y(\theta) = e^{-i\theta\hat{J}_y}; \quad R_z(\psi) = e^{-i\psi\hat{J}_z}$$

where  $\hat{J}_x, \hat{J}_y, \hat{J}_z$  are the angular momentum operators of a spin- $\frac{1}{2}$  particle [1].

The angular momentum operators are represented using the Pauli matrices:

$$\hat{J}_x = \frac{\hbar}{2}\sigma_x, \quad \hat{J}_y = \frac{\hbar}{2}\sigma_y, \quad \hat{J}_z = \frac{\hbar}{2}\sigma_z$$

where  $\hbar$  is Planck's constant.

Thus, the rotation operator for spin- $\frac{1}{2}$  is:

$$R_x(\phi) = e^{-i\frac{\phi}{2}\sigma_x}, \quad R_y(\theta) = e^{-i\frac{\theta}{2}\sigma_y}, \quad R_z(\psi) = e^{-i\frac{\psi}{2}\sigma_z}$$

Expanding the exponentials using the identity, for any rotational angle  $\alpha$ ,

$$e^{-i\frac{\alpha}{2}\hat{\sigma}_i} = \cos\left(\frac{\alpha}{2}\right)I - i\sin\left(\frac{\alpha}{2}\right)\sigma_i \quad (1)$$

where  $I$  is the Identity matrix.

We obtain the individual rotation matrices:

$$R_x(\phi) = \begin{bmatrix} \cos\left(\frac{\phi}{2}\right) & -i\sin\left(\frac{\phi}{2}\right) \\ -i\sin\left(\frac{\phi}{2}\right) & \cos\left(\frac{\phi}{2}\right) \end{bmatrix} \quad (2)$$

$$R_y(\theta) = \begin{bmatrix} \cos\left(\frac{\theta}{2}\right) & -\sin\left(\frac{\theta}{2}\right) \\ \sin\left(\frac{\theta}{2}\right) & \cos\left(\frac{\theta}{2}\right) \end{bmatrix} \quad (3)$$

$$R_z(\psi) = \begin{bmatrix} e^{-i\psi/2} & 0 \\ 0 & e^{i\psi/2} \end{bmatrix} \quad (4)$$

Quantum rotation matrices satisfy some properties like [14]:

- **Unitarity:**

$$\hat{R}^\dagger \hat{R} = I$$

where  $\dagger$  is the dagger operation.

- **Non-commutativity:** Rotations do not generally commute in quantum mechanics.

$$[R_i, R_j] \neq 0$$

Our proposed EQNN model contains three parts: data encoding, gated quantum circuit, and measurement. We use a 16-qubit quantum circuit, as shown in Fig. 4, where each wire represents a single-qubit.

#### A. Data Encoding

The unitary matrix is a fundamental concept in quantum mechanics. In this work, we utilize the SU(2) representation of the Rotational-X operator as the basis for our encoding technique. Various encoding methods are available in quantum computing, like amplitude encoding, basis encoding, and binary encoding [8]. Our approach employs angle encoding, which maps classical data into quantum states using a Rotational- $x$  matrix, denoted as  $R_x(\theta)$  in eq. (2). In this formulation, the parameter  $\theta$  represents the classical data encoded into the quantum state. The quantum state is expressed as a linear combination of the computational basis states  $|0\rangle$  and  $|1\rangle$ . For  $n$  classical data points  $[x_1, x_2, \dots, x_n]^T \in \mathbb{R}^1$ , the encoded quantum state can be represented as:

$$|\Psi\rangle = \bigotimes_{i=1}^n (a_i |0\rangle + b_i |1\rangle), \quad (5)$$

where  $\bigotimes$  is a tensor product and each qubit corresponds to a linear combination of  $|0\rangle$  and  $|1\rangle$ , with coefficients  $a_i \in \mathbb{C}, b_i \in \mathbb{C}$

To simplify mathematical operations, the quantum state  $|\Psi\rangle$  is alternatively expressed in the density matrix formalism. The density matrix  $\rho$  for any state is given by  $|\Psi\rangle\langle\Psi|$ :

$$\rho = \left( \bigotimes_{i=1}^n (a_i |0\rangle + b_i |1\rangle) \right) \left( \bigotimes_{i=1}^n (a_i^* \langle 0| + b_i^* \langle 1|) \right). \quad (6)$$

Through this angle encoding method, we ensure that the structural information of the complex data is preserved after encoding it into quantum states.

#### B. Gated Circuit

In this paper, we introduce our novel quantum circuit architecture. The novelty of a quantum circuit is evaluated based on three key aspects: expressibility, entanglement, and computational cost of the circuit.

The expressibility of a quantum circuit measures its ability to effectively and uniformly span a given state space, typically represented by the Hilbert space. For a single-qubit state, this corresponds to spanning the Bloch sphere shown in Fig. 2.

Evaluating the entanglement generation of a quantum circuit is crucial, especially in applications related to quantum computing and quantum information processing. The entanglement entropy of a quantum system quantifies the degree of entanglement between its subsystems. For a pure state  $|\psi\rangle$  of a composite system partitioned into subsystems  $A$  and  $B$ , the

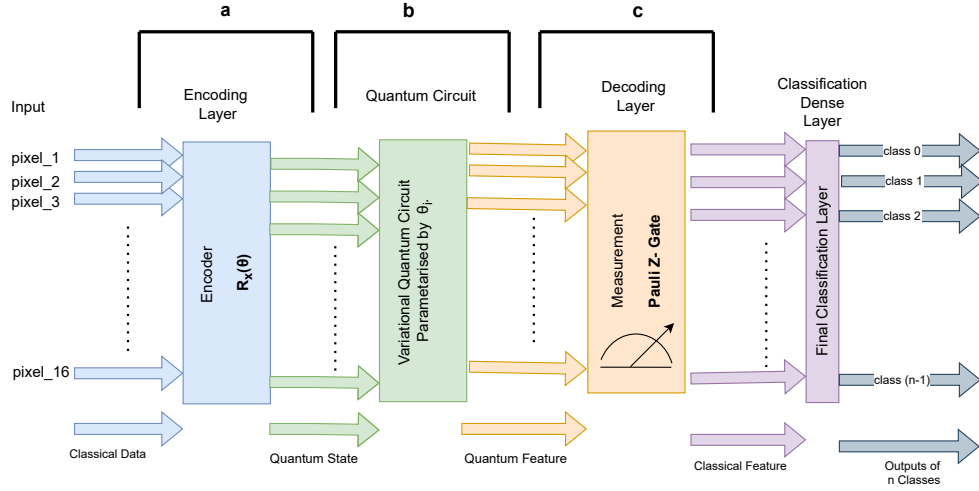


Fig. 1. Diagram of the proposed Eulerian Quantum Neural Network (EQNN). It has three main components: (a) Data encoding, where classical data is mapped to quantum states; (b) Quantum gated circuit, which processes the encoded data using a series of quantum gates; and (c) Measurement and final classification, where the quantum states are measured and the results are interpreted for classification.

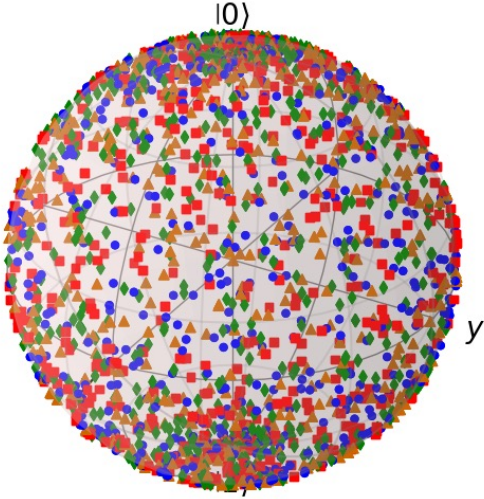


Fig. 2. Single-qubit Bloch-sphere representation using the Euler angle rotation.

entanglement entropy is defined as the Von Neumann entropy of the reduced density matrix of either subsystem:

- The total pure state  $|\Psi\rangle$  is associated with a density matrix  $\rho = |\Psi\rangle\langle\Psi|$ .
- The reduced density matrix for the subsystem  $A$  is obtained via the partial trace over the subsystem  $B$ :

$$\rho_A = \text{Tr}_B(\rho),$$

where  $\text{Tr}_B$  denotes the partial trace operation over subsystem  $B$ .

- The entanglement entropy is then given by:

$$S(\rho_A) = -\text{Tr}(\rho_A \log \rho_A),$$

where  $\text{Tr}$  denotes the trace operator.

A higher value of  $S(\rho_A)$  corresponds to greater entanglement between the subsystems  $A$  and  $B$ .

The computational cost of a quantum circuit can be quantified by analyzing the number of single-qubit gates, multi-qubit gates, and the circuit depth. In our design, the quantum circuit consists of three layers, with the following configuration for each layer:

- **Single-qubit Gates:** Each layer contains 48 parameterized single-qubit rotation gates,  $R_x$  and  $R_z$ .
- **Two-qubit Gates:** Each layer includes 15 two-qubit gates, implemented as Controlled-Z ( $CZ$ ) gates.

The depth of the circuit for the three-layer architecture is 3. The total number of gates and are calculated as follows:

$$\text{Single-qubit parameterized gates} = 3 \times 48 = 144,$$

$$\text{Two-qubit gates} = 3 \times 15 = 45,$$

Rotations in 3D space can be represented by elements of the  $\text{SU}(3)$  group. An arbitrary 3D rotation can be expressed as a combination of three rotations about the principal axes ( $x$ -,  $y$ -, and  $z$ -axes). Specifically, the composition  $R_z R_y R_z$  corresponds to a proper Euler angle parameterization of rotations. This sequence, referred to as the ZYZ Euler angle parameterization, is detailed as follows:

- **First:**  $R_z(\phi)$ : A rotation about the  $z$ -axis by an angle  $\phi$ .
- **Then:**  $R_y(\theta)$ : A rotation about the  $y$ -axis by an angle  $\theta$ .

- **Finally:**  $R_z(\psi)$ : A rotation about the  $z$ -axis by an angle  $\psi$ .

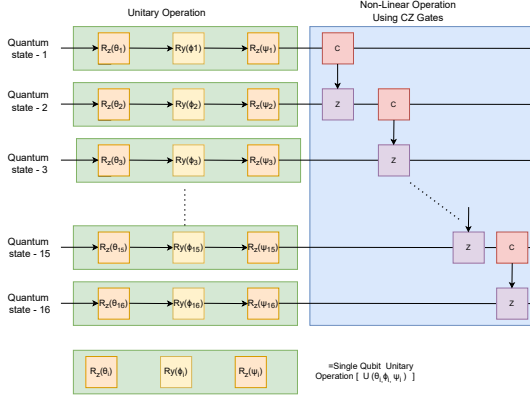


Fig. 3. Schematic diagram of the gated quantum circuit. Here,  $R_z(\theta)$ ,  $R_y(\phi)$ ,  $R_z(\psi)$  are single-qubit parameterized rotational gates, and  $CZ$  is a two-qubit Controlled- Pauli-Z gate.

In quantum computing, unitary transformations are essential for manipulating quantum states because it preserves probability states. These transformations can be represented as a sequence of rotations around specific axes. The general single-qubit rotational matrix obtained from Euler angle rotation is expressed as:

$$U(\theta, \phi, \psi) = R_z(\phi)R_y(\theta)R_z(\psi), \quad (7)$$

where  $R_z$  and  $R_y$  are rotation matrices around the  $z$ - and  $y$ -axes, respectively.

Performing the matrix multiplication gives:

$$U(\theta, \phi, \psi) = \begin{bmatrix} \cos\left(\frac{\theta}{2}\right)e^{-i\frac{\phi+\psi}{2}} & -\sin\left(\frac{\theta}{2}\right)e^{-i\frac{\phi-\psi}{2}} \\ \sin\left(\frac{\theta}{2}\right)e^{i\frac{\phi-\psi}{2}} & \cos\left(\frac{\theta}{2}\right)e^{i\frac{\phi+\psi}{2}} \end{bmatrix} \quad (8)$$

We compute its Hermitian conjugate  $U^\dagger(\theta, \phi, \psi)$ :

$$U^\dagger(\theta, \phi, \psi) = ((U(\theta, \phi, \psi))^*)^T \quad (9)$$

and we obtain

$$U^\dagger U = I \quad (10)$$

Thus,  $U(\theta, \phi, \psi)$  is a unitary matrix of our system. The parameterization using three Euler angle rotations—comprising rotations about the  $z$ -axis,  $y$ -axis, and again the  $z$ -axis—results in a final unitary transformation. Such a parameterization is utilized in our quantum circuit, represents general single-qubit gates while preserving the fundamental properties of quantum mechanics.

In our quantum circuit, two-qubit Controlled-Z (CZ) gates are employed to introduce entanglement, thereby inducing non-linearity within the quantum circuit model and facilitating the development of complex quantum correlations. This entanglement provides insights into the degree of classical correlation between pixels, analogous to local interactions

among pixels. Furthermore, two-qubit entangling gates are both sufficient and cost-effective for processing small-size images.

### C. Measurement of Quantum Circuit

In quantum mechanics, when a quantum state  $|\phi\rangle$  is measured with respect to an operator  $O$  (typically a Hermitian operator representing an observable), the measurement process is described as follows:

The measurement of  $|\phi\rangle$  with respect to  $O$  yields the expectation value, which represents the average outcome of the measurement over many trials. The expectation value is given by:

$$\langle O \rangle = \langle \phi | O | \phi \rangle, \quad (11)$$

where  $\langle \phi |$  is the conjugate transpose (dual state) of  $|\phi\rangle$ .

Then for a fixed state, density matrix representation is given by:  $\rho = |\phi\rangle\langle\phi|$ .

The expectation value of the measurement of  $O$  can be expressed in terms of the density matrix as:

$$\langle O \rangle = \text{Tr}(\rho O), \quad (12)$$

The expectation value simplifies to:

$$\langle O \rangle = \text{Tr}(|\phi\rangle\langle\phi|O) = \langle \phi | O | \phi \rangle. \quad (13)$$

In this framework, the Pauli-Z matrix is utilized as the measurement operator ( $O$ ). This operator serves to project the quantum states into the desired classical data representation. The application of the Pauli-Z matrix facilitates the extraction of meaningful classical information from quantum states, enabling a mapping between the quantum and classical domains.

## IV. RESULTS AND DISCUSSION

We utilize three benchmark datasets: MNIST, Fashion MNIST (F-MNIST), and Pneumonia-MNIST. The MNIST dataset comprises 10 classes with 60,000 images for training and 10,000 images for testing, each shaped as  $[28, 28, 1]$ . It contains grayscale images of handwritten digits. Similarly, the F-MNIST dataset consists of 60,000 training images and 10,000 testing images of clothing items such as shirts and shoes. The PneumoniaMNIST(P-MNIST) is based on a prior dataset of 5,856 pediatric chest X-Ray images. The task is binary-class classification of pneumonia against normal. The source training set is split with a ratio of 9:1 into training and validation set, and use its source validation set as the test set. The source images are gray-scale, and their sizes are  $(384-2,916) \times (127-2,713)$ . The images are center-cropped with a window size of length of the short edge and resized into  $1 \times 28 \times 28$ . For the purpose of our experiments, all images are resized to  $[4, 4, 1]$ .

We conducted our simulations on the Google Colab platform using TensorFlow Quantum (version 0.7.3) and Cirq. TensorFlow Quantum, which facilitates hybrid quantum-classical ML models, is incompatible with GPU platforms; hence, all our models were simulated on CPUs. Cirq, an open-source library developed by Google, was employed for quantum circuit development. The Parameterized Quantum

Circuit layer of TensorFlow Quantum was used in our models.

For training, we have used two methods, selecting 500 and 1000 images from each class, while 1000 testing images were used for evaluation of MNIST and F-MNIST and 624 for P-MNIST. After resizing, the images were flattened into arrays of shape  $[16, 1]$ . These arrays served as inputs to our model, which processed the data in batches. We performed both two-class and three-class classifications on all three datasets. The results, including accuracy, precision, F1 score, and recall, for different models and classifications are summarized in Table I.

TABLE I  
PERFORMANCES FOR DIFFERENT DATASETS ON TWO-CLASS AND THREE-CLASS CLASSIFICATIONS. ALL SCORES ARE IN %.

| Dataset | Classes | Samples | Acc   | Pre   | Rec   | F1    |
|---------|---------|---------|-------|-------|-------|-------|
| MNIST   | 2       | 500     | 96.30 | 96.30 | 96.30 | 96.30 |
| MNIST   | 2       | 1000    | 96.40 | 96.40 | 96.40 | 96.40 |
| MNIST   | 3       | 500     | 78.00 | 80.00 | 78.00 | 78.00 |
| MNIST   | 3       | 1000    | 79.00 | 80.00 | 79.00 | 77.00 |
| F-MNIST | 2       | 500     | 81.30 | 81.42 | 81.30 | 81.30 |
| F-MNIST | 2       | 1000    | 77.30 | 77.96 | 77.30 | 77.23 |
| F-MNIST | 3       | 500     | 75.10 | 77.57 | 75.10 | 75.22 |
| F-MNIST | 3       | 1000    | 74.00 | 77.76 | 74.00 | 74.04 |
| P-MNIST | 2       | 500     | 82.53 | 82.38 | 82.53 | 82.41 |
| P-MNIST | 2       | 1000    | 82.21 | 82.07 | 82.53 | 82.41 |

Table I showcases the performance of the EQNN across MNIST, F-MNIST, and P-MNIST datasets for two-class and three-class classification tasks, using 500 and 1000 training samples. On MNIST, the EQNN achieved its highest accuracy of 96.40% for two-class classification and 79.00% for three-class classification with 1000 samples, showing improved performance with larger datasets. For F-MNIST, the model obtained 81.30% accuracy for two-class classification and 75.10% for three-class classification with 500 samples, with a slight decline when using 1000 samples, reflecting the complexity of the dataset. P-MNIST showed consistent results, achieving 82.53% accuracy for two-class classification with 500 samples and a marginal drop to 82.21% with 1000 samples.

Table II highlights the performance of our proposed EQNN model compared to recent state-of-the-art methodologies on the MNIST and F-MNIST datasets. The results demonstrate the competent performance of the EQNN, particularly in its ability to effectively encode and classify image data using optimized quantum representations.

For the MNIST dataset, EQNN achieved an accuracy of 96.30% for two-class classification, surpassing the 95.80% reported by Philip et al., 2024, which utilized a 4x4 patch-based feature extraction approach using single qubit unitary operator. Similarly, for three-class classification on MNIST, EQNN significantly outperformed the baseline by achieving an accuracy of 78.00% compared to 72.10%, attributed to its improved feature encoding through unitary transformations and efficient quantum state representation.

On the Fashion MNIST dataset, for two-class classification, EQNN achieved an accuracy of 81.30% compared to 89.50% by Philip et al., 2024. While EQNN's accuracy was slightly lower, it utilized a more efficient quantum state preparation technique, demonstrating its potential for further optimization in datasets with high variability and complexity. Figure ??? presents the performance of the EQNN model on the MNIST dataset for two-class and three-class classifications. The confusion matrices on the left and center show the classification results, while the t-SNE visualization on the right illustrates the separability of the quantum layer output features.

We employed the EQNN model to evaluate its performance on three datasets: MNIST, Fashion-MNIST (F-MNIST), and the Pneumonia dataset (P-MNIST). The figure summarizes the results, with confusion matrices displayed in the top row and t-SNE visualizations of the quantum layer's output features in the bottom row. Each column corresponds to one dataset, allowing a direct comparison of the EQNN's performance across different levels of complexity.

The confusion matrices provide a clear view of the EQNN's classification performance. For the MNIST dataset, the confusion matrix (a) reflects strong accuracy, with the majority of samples accurately classified. Class 1 (digit '1') is particularly well-predicted, with 341 samples correctly classified and minimal misclassification. However, some overlap is observed between Class 0 (digit '0') and Class 2 (digit '2'), indicating areas for improvement in distinguishing these two categories. For the F-MNIST dataset, the confusion matrix (b) shows a slight decline in performance. Misclassifications are more prominent, particularly between Class 0 (T-shirt/top) and Class 1 (trouser), highlighting the dataset's increased complexity and the challenge of distinguishing fine-grained fashion categories. The Pneumonia dataset, depicted in confusion matrix (c), presents the greatest challenge. The results show significant misclassification between the two classes, demonstrating the difficulty of capturing subtle features in pneumonia-related medical imaging.

The t-SNE plots provide further insight into the separability of features learned by the EQNN's quantum layers. For the MNIST dataset, the t-SNE visualization (d) displays distinct and well-separated clusters for each class, reflecting the quantum layer's ability to effectively extract discriminative features. This supports the high classification accuracy observed in the corresponding confusion matrix. In contrast, the t-SNE plot for the F-MNIST dataset (e) reveals less distinct clusters, with visible overlap between certain classes, such as Class 0 (T-shirt/top) and Class 1 (trouser). This overlap aligns with the moderate decline in performance, as shown in the confusion matrix for F-MNIST.

The t-SNE visualization for the Pneumonia dataset (f) exhibits substantial feature overlap, with the two classes forming entangled clusters. This lack of clear separability highlights the inherent complexity of pneumonia-related medical images. The subtle patterns in these images make it challenging to extract distinguishing features, even for advanced models like EQNN. This visualization corroborates the lower accuracy

observed in the Pneumonia dataset’s confusion matrix, emphasizing the dataset’s complexity and the need for further refinement in feature extraction and classification.

In summary, the EQNN demonstrates strong performance on simpler datasets like MNIST, where feature clusters are well-separated, leading to high classification accuracy. However, the increasing complexity of F-MNIST and the Pneumonia dataset introduces challenges, resulting in reduced accuracy and more entangled feature representations. The confusion matrices and t-SNE visualizations together provide a comprehensive understanding of EQNN’s capabilities and limitations across datasets of varying complexity. These results emphasize the effectiveness of the EQNN in leveraging Euler angle rotations for high-fidelity data representation with minimal qubit requirements. By optimizing feature encoding and efficiently modeling geometric and rotational transformations, the EQNN demonstrates robust performance, scalability, and reliability across binary and multi-class classification tasks in quantum machine learning.

## V. CONCLUSION AND FUTURE SCOPE

This paper proposes a lightweight and efficient EQNN QML model for image classification, leveraging the strengths of quantum computing to overcome challenges faced by classical DL models. Our results demonstrate that the proposed model achieves competent accuracy while utilizing minimal computational resources, thereby making it well-suited for real-time applications. However, the current implementation, which utilizes only 16 qubits, is limited to grayscale images. Additionally, the use of angle encoding, while effective to some extent, may not fully capture classical information in the quantum domain, potentially leading to performance degradation for complex image classification tasks. Measurement limitations, such as reliance on the Pauli-Z gate, could further impact the model’s accuracy. Future research will focus on scaling the model to accommodate larger datasets and exploring advanced encoding schemes, including hybrid encoding techniques, to improve information representation and model performance across diverse applications.

## ACKNOWLEDGMENT

The authors would like to thank the Centre for Micro-processor Applications for Training, Education and Research (CMATER) laboratory of the Computer Science and Engineering Department, Jadavpur University, Kolkata, India, for providing the infrastructural support.

## REFERENCES

- [1] Yakir Aharonov, David Z Albert, and Lev Vaidman. How the result of a measurement of a component of the spin of a spin-1/2 particle can turn out to be 100. *Physical review letters*, 60(14):1351, 1988.
- [2] Avinash Chalumuri, Raghavendra Kune, S Kannan, and BS Manoj. Quantum-enhanced deep neural network architecture for image scene classification. *Quantum Information Processing*, 20(11):381, 2021.
- [3] Iris Cong, Soonwon Choi, and Mikhail D Lukin. Quantum convolutional neural networks. *Nature Physics*, 15(12):1273–1278, 2019.
- [4] Alexey Dosovitskiy. An image is worth 16x16 words: Transformers for image recognition at scale. *arXiv preprint arXiv:2010.11929*, 2020.
- [5] Philip Easom-McCaldin, Ahmed Bouridane, Ammar Belatreche, Richard Jiang, and Somaya Al-Maadeed. Efficient quantum image classification using single qubit encoding. *IEEE Transactions on Neural Networks and Learning Systems*, 35(2):1472–1486, 2022.
- [6] David J Griffiths and Darrell F Schroeter. *Introduction to quantum mechanics*. Cambridge university press, 2019.
- [7] Maxwell Henderson, Samridhi Shakya, Shashindra Pradhan, and Tristan Cook. Quantvolutional neural networks: powering image recognition with quantum circuits. *Quantum Machine Intelligence*, 2(1):2, 2020.
- [8] Ryan LaRose and Brian Coyle. Robust data encodings for quantum classifiers. *Physical Review A*, 102(3):032420, 2020.
- [9] Natansh Mathur, Jonas Landman, Yun Yvonna Li, Martin Strahm, Skander Kazdaghli, Anupam Prakash, and Iordanis Kerenidis. Medical image classification via quantum neural networks. *arXiv preprint arXiv:2109.01831*, 2021.
- [10] David Peral-García, Juan Cruz-Benito, and Francisco José García-Peñalvo. Systematic literature review: Quantum machine learning and its applications. *Computer Science Review*, 51:100619, 2024.
- [11] Nisheeth Saxena and Akriti Nigam. Performance evaluation of a variational quantum classifier. In *2022 IEEE 9th Uttar Pradesh Section International Conference on Electrical, Electronics and Computer Engineering (UPCON)*, pages 1–5, 2022.
- [12] Nisheeth Saxena and Akriti Nigam. Performance evaluation of a variational quantum classifier. In *2022 IEEE 9th Uttar Pradesh Section International Conference on Electrical, Electronics and Computer Engineering (UPCON)*, pages 1–5. IEEE, 2022.
- [13] Sukin Sim, Peter D Johnson, and Alán Aspuru-Guzik. Expressibility and entangling capability of parameterized quantum circuits for hybrid quantum-classical algorithms. *Advanced Quantum Technologies*, 2(12):1900070, 2019.
- [14] Gilbert Strang. *Introduction to linear algebra*. SIAM, 2022.

TABLE II  
COMPARISON OF THE EQNN WITH RECENT METHODS ON VARIOUS DATASETS USING 500 TRAINING SAMPLES.

| Dataset | Work Ref.           | Classes | Accuracy (%) | Remarks  |
|---------|---------------------|---------|--------------|--|
| MNIST   | Philip et al., 2024 | 2       | 95.80        | Features extracted from 4×4 patches using single-qubit unitary matrix from (12×12) image |
|         | <b>EQNN</b>         | 2       | <b>96.30</b> | Optimized quantum feature representation   |
|         | Philip et al., 2024 | 3       | 72.10        | Features extracted from 3×3 patches  |
|         | <b>EQNN</b>         | 3       | <b>78.00</b> | Improved feature encoding via Eulerian unitary transformation                            |
| F MNIST | Philip et al., 2024 | 2       | 89.50        | 3×3 patch-based preprocessing  |
|         | <b>EQNN</b>         | 2       | <b>81.30</b> | Efficient quantum state preparation  |

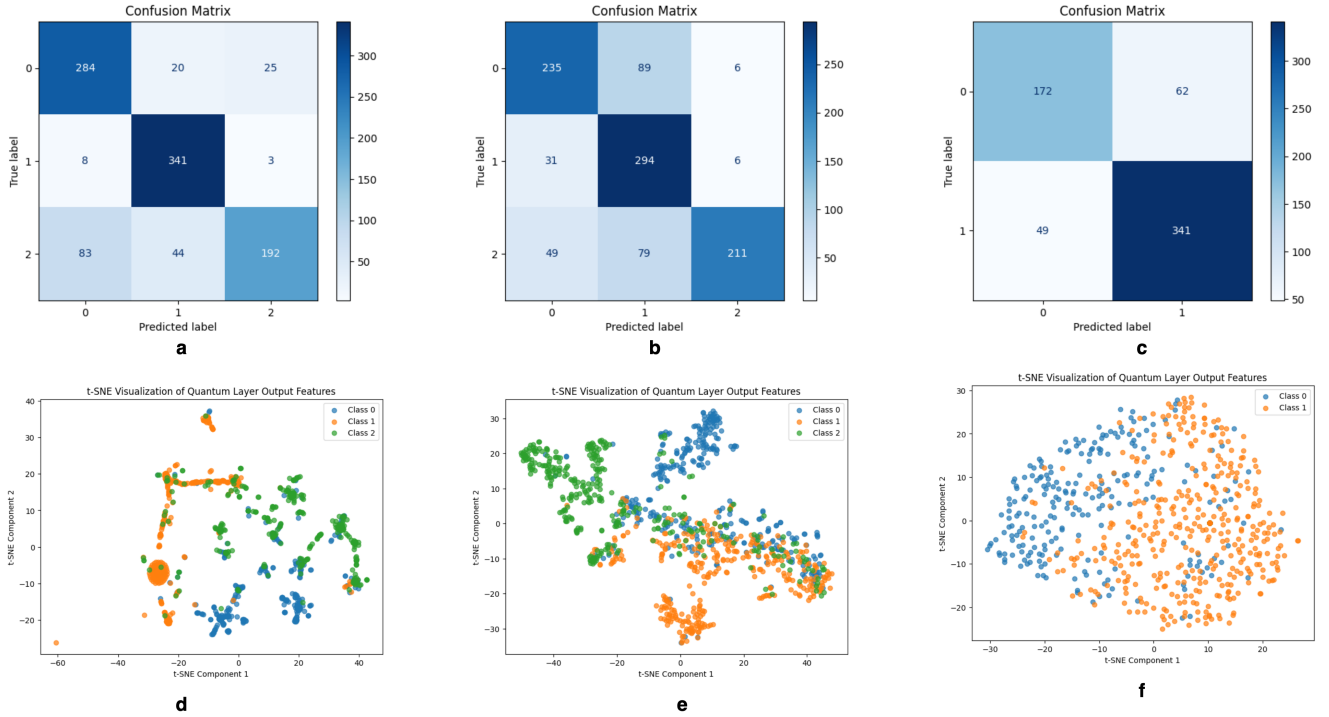


Fig. 4. Performance evaluation of the EQNN on MNIST, F-MNIST, and P-MNIST datasets. (a), (b), and (c) show confusion matrices for MNIST, F-MNIST, and P-MNIST datasets, respectively. (d), (e), and (f) display the corresponding t-SNE visualizations of the quantum layer output features, illustrating feature separability for each dataset.